Unraveling the Origin of Enhanced Safety in Capacitive Type Carbon Electrode for 20 C Sodium-Ion Capacitors

Bo Xiong[1], Jieming Cai[1], Biao Zhong[1], Luoming Zhang[1], Dongxiao Li[1], Jie Li[1], Juan Tian[2], Xiongwei Luo[2], Fei Yao[2], Zhiyu Zeng[2], Wentao Deng[1], Hongshuai Hou[1], Jialuo She[3], Tianyun Qiu*[4], Guoqiang Zou*[1], Dulin Yin[3], and Xiaobo Ji[1]*

[1] College of Chemistry and Chemical Engineering, Central South University, Changsha, 410083, Hunan, China.

[2] Hunan Changlian New Material Technology Co., Ltd.

[3] National & Local United Engineering Laboratory for New Petrochemical Materials & Fine Utilization of Resources, College of Chemistry and Chemical Engineering, Hunan Normal University.

[4] School of Photovoltaic and Renewable Energy Engineering, UNSW Sydney, Australia.

Corresponding Author

* Email address: dingbang53191@163.com, tianyun.qiu@unsw.edu.au and gq-zou@csu.edu.cn

1. Materials synthesis

The coal tar materials used in this study were purchased from Hunan Changlian New Material Technology Co. The phosphorus source (NaH_2PO_4) and coal tar were mixed in a mass ratio of 1:9. The mixture was heated at a rate of 5 ℃ min^{-1} under a nitrogen atmosphere to 200 ℃ and held at this temperature for 5 hours. It was then heated at a rate of 2 ℃ min^{-1} under a nitrogen atmosphere to 500 ℃, maintained at this temperature for 2 hours, yielding the precursor phosphorus-doped coal tar (PCT). Then PCT was heated in a tube furnace under Ar atmosphere at 700, 800, 900, 1000, and 1200 ℃ for 2 h with a heating rate of 5 ℃ min^{-1} and an airflow rate of 50 ml min^{-1}, and the carbonized and synthesized material was named as

PCT-X (X stands for the different carbonization temperatures). For comparison, the undoped coal tar CT was annealed and carbonized in the same way at 800 ℃ to obtain a sample noted as CT-800.

2. Materials Characterizations

The structure of the samples was characterized by CU-Kα radiation (λ = 1.54 Å) using an X-ray powder diffractometer (XRD, Rigaku Ultima) operating at 40 kV and 250 mA. The microstructure of the samples was explored by scanning electron microscopy (SEM, JEOL/JSM-7610FPLUS) and transmission electron microscopy (TEM, JEOL JEM 2100F). Defect structures were determined on a Raman spectrometer (RENISHAW invia, 532 nm excitation). The BET specific surface area and pore size distribution of the samples were determined by a Micromeritics ASAP 2020 instrument using N_2 (77 K).TG was measured by a thermogravimetric analyzer (STA449F3) with a heating rate of 5 ℃ min^{-1} in Ar. X-ray photoelectron spectroscopy (XPS) spectra were recorded by Thermo Scientific K-Alpha) spectra. Powder tap density was measured using a ZS-102 tap density tester. Infrared spectra were tested with a FTIR spectrometer (AVTA-TAR 370).

L_a: lateral size of the crystallite can be calculated by the following equation: L_a (nm)=$K\lambda/\beta\sin\theta$ (K=0.89, β is half width of (100) diffraction peak, λ=1.54Å).

L_c: stacking height of the crystallite can be calculated by the following equation: L_c (nm)= $K\lambda/\beta\cos\theta$ (K=0.89, β is half width of (002) diffraction peak, λ=1.54Å).

d: layer spacing can be calculated by Bragg equation: $d = n\lambda/2\sin\theta$, θ is the incoming ray, the included angle between the reflection ray and the reflected crystal plane, λ is the wavelength, n refers to the reflection series.

3. Electrochemical Measurements

Electrochemical behavior measurements were performed on a coin cell (CR2016). The working electrode was fabricated by the slurry method, in which synthetic soft carbon was used as the active material, sodium carboxymethyl cellulose (CMC, Sigma-Aldrich) as the binder, and Super P Li (Tianjin Avexin Chemical Technology) as the binder, dissolved in water in the ratio of 7:1.5:1.5 by weight with oscillating and stirring for 6 h. The slurry was uniformly coated onto a copper foil substrate and then dried at 80 ℃ in a vacuum oven for 8 h.

The electrode was cut into 14-mm diameter discs to obtain the negative electrode, and the active material loaded with about 1 mm was used. The anode was obtained by cutting the electrode into 14 mm diameter discs with an active substance loading of about 0.8-1.2 mg cm^{-2}. Glass fiber (Whatman, type GF/D) was used as a diaphragm. The sodium metal (Aladdin) with a thickness of about 1 mm and a diameter of 16 mm served as the counter electrode, which was assembled with the working electrode to form a half-cell. The ether-based electrolyte was 1 M NaPF6 in DIGLYME 100% (NP005) and 300 μL of electrolyte was used for each half-cell test. Constant current charge/discharge tests and constant current intermittent titration technique (GITT) tests were performed on the LAND Test System within 0-3 V (vs Na^+ /Na) at room temperature. For the cycling performance test, the cells were fully rested for 6 h and then activated with 0.03 A g^{-1} current for 2 cycles, followed by constant current charge/discharge test at 0.1 A g^{-1}. For the rate capability test, 5 cycles at 0.05, 0.1, 0.2, 0.5, 1, and 2 A g^{-1} were performed sequentially after fully resting for 6 h, followed by the test at 0.1 A g^{-1}. The GITT test was performed with a current density of 0.02 A g^{-1} in the range of 0-2.8 V for 15 min per charge/discharge, standing time for 1 h subsequently. Electrochemical impedance spectroscopy (EIS) was performed on a Chenhua electrochemical workstation (CHI660D) with a frequency range of 10^{-2} to 10^5 Hz. Cyclic voltammetry (CV) tests were performed between 0 and 3 V at 0.2, 0.4, 0.6, 0.8, 1.0 mV s^{-1} by an electrochemical workstation (Autolab M204). The voltage profiles were measured with five different current densities of 0.1, 0.5, 1, 2, 5 A g^{-1} to measure the energy and power densities of the sodium ion capacitors.

In-situ Raman was performed by a Raman instrument (Horiba, Horiba LabRAM HR Evolution, France) coupled to an electrochemical workstation (Bio-logic VMP3, France). In-situ XRD was characterized by CU-Kα radiation (λ=1.54 Å) by an X-ray powder diffractometer (XRD, Rigaku Ultima) operating at 40 kV and 50 mA. The ex-situ XRD and XPS were performed by disassembling the half-cells that were charged to different potentials, and the pole pieces were cleaned with dimethyl carbonate (DMC) and then tested separately.

In addition, half-cells, button full-capacitors, and pouch cells (the mass ratio of anode and cathode active substances is about 2.7:1) were fabricated using sodium ferric pyrophosphate

(NFPP, Shenzhen OME.com) as the cathode, and electrochemical characterizations, such as CV tests and cycling performance, were carried out in the voltage range 1.0-4 V.

4. Theoretical calculations

The first-principles calculations were performed by using the projector augmented wave (PAW) method within the density functional theory (DFT) as implemented in the Cambridge Serial Total Energy Package (CASTEP) code. The electronic exchange-correlation function was treated within the spin-polarized generalized gradient approximation (GGA) parameterized by Perdew-Burke-Ernzerhof (PBE).

The kinetic energy cutoff was set to 450 eV for the plane-wave basis set. Brillouin zone integration was sampled with 2 × 2 × 1 Monkhorst Pack mesh k-point for pristine monolayer graphene (MC), phosphorus-doped graphene featuring P-C bonds (MPC) and phosphorus-doped graphene featuring P-O-C bonds (MPOC). The convergence tolerances were set to be 2 × 10^{-5} eV per atom for energy, 2 × 10^{-3} Å for maximum displacement, and 0.05 eV/Å for maximum force. All of the structures were fully optimized and relaxed to the ground state. The long-range van der Waals (vdWs) interaction was corrected by DFT-D method.

The adsorption energy (E_{ad}) was defined using equation (5)

$$E_{ad} = E_{Na/support} - (E_{Na} + E_{support}) \quad (5)$$

Where E_{ad} is the adsorption energy, the $E_{Na/support}$, E_{Na} and $E_{support}$ are the total energies of one Na^+ adsorbed at the surface of support, one Na atom in the same slab and the clean surface of support, respectively.

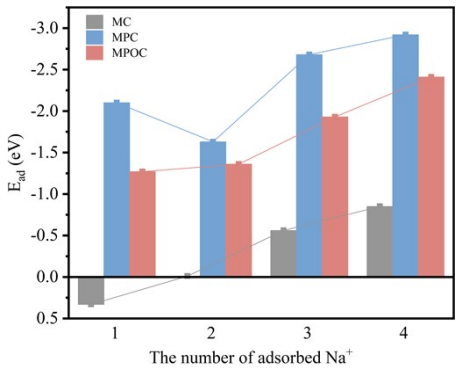

Figure S1. the E_{ad} on MC, MPC, and MPOC with varying numbers of Na^+.

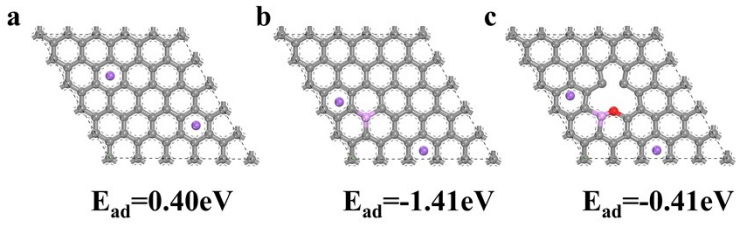

Figure S2. the E_{ad} on MC, MPC, and MPOC with two non-interacting adsorbed Na^+.

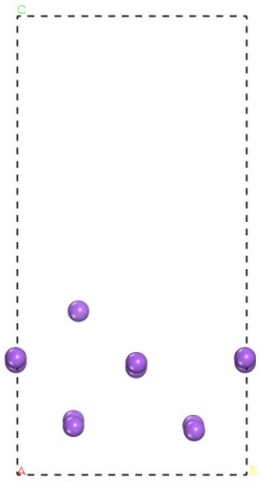

Figure S3. Adsorption of Na^+ by Na^+ (E_{ad}=-1.42eV).

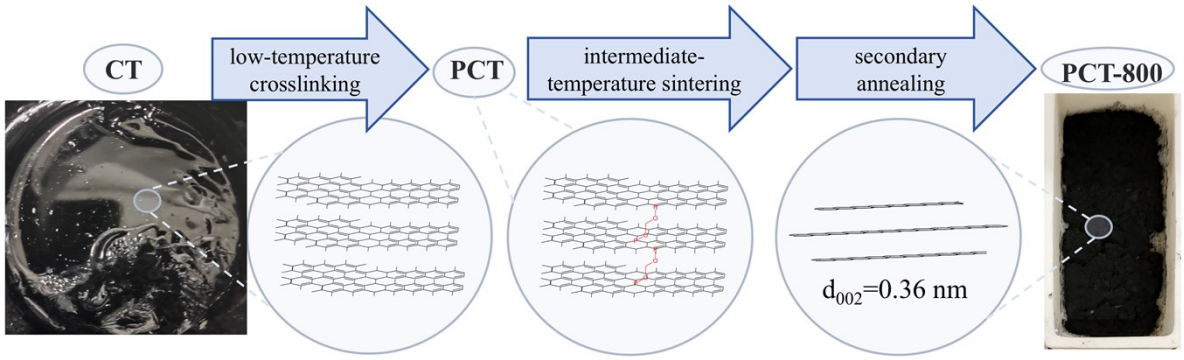

Figure S4. Schematic diagram of the preparation process of coal tar-derived carbon materials.

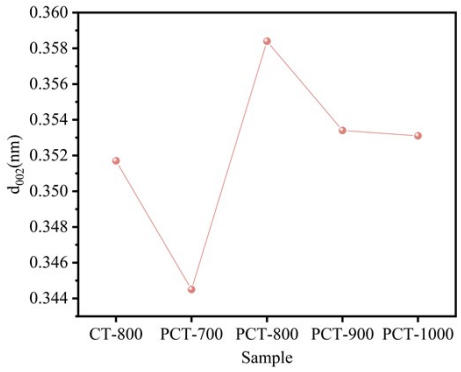

Figure S5. d_{002} of the as-prepared sample.

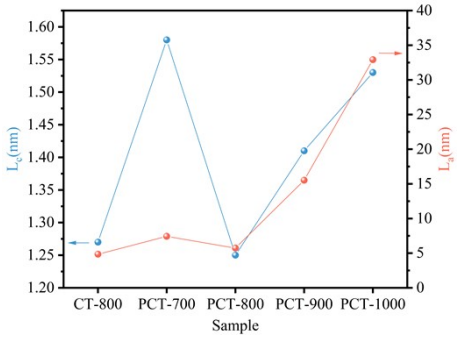

Figure S6. L_a and L_c values of the as-prepared sample.

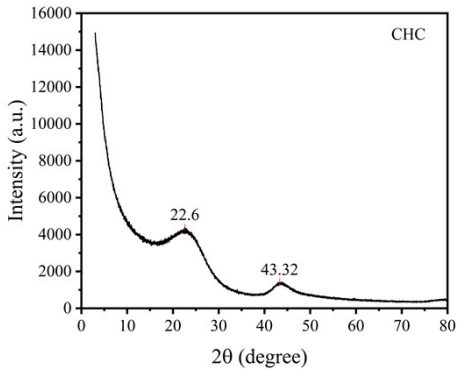

Figure S7. XRD pattern of CHC.

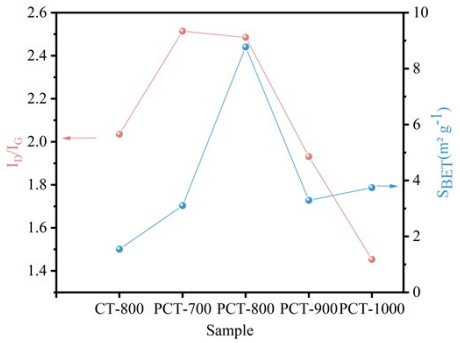

Figure S8. I_D/I_G and specific surface area.

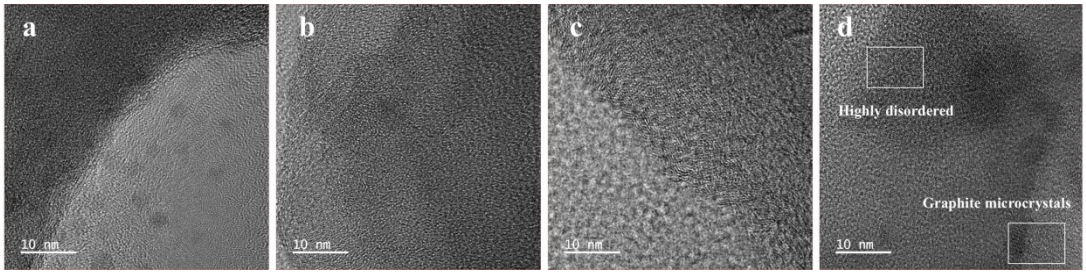

Figure S9. TEM image of (a) PCT-700; (b) CT-900; (c) PCT-1000; (d) PCT-800.

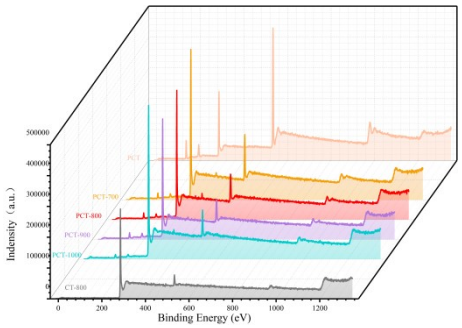

Figure S10. XPS survey spectra of PCT-X samples.

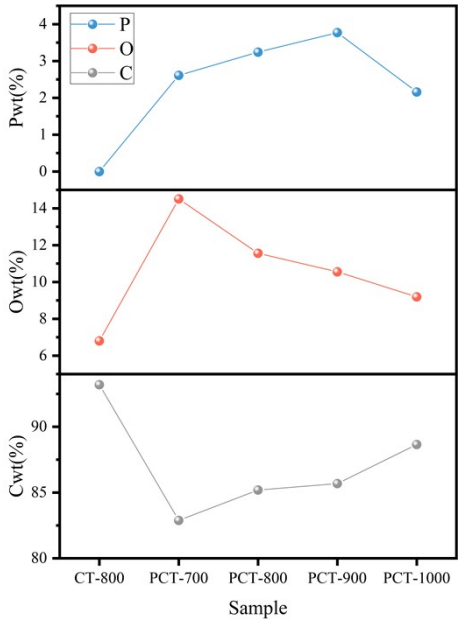

Figure S11. Percentage elemental composition of PCT-X samples.

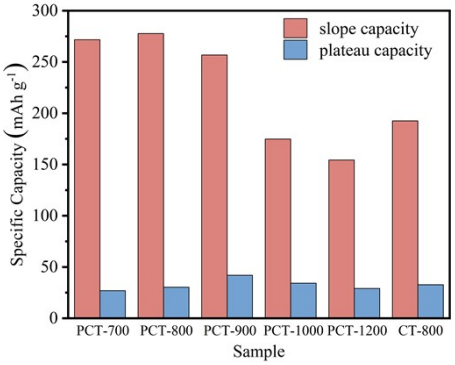

Figure S12. Slope capacity and plateau capacity of PCT-X samples.

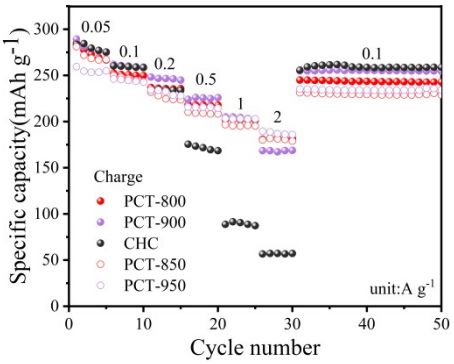

Figure S13. Comparison of the rate performance.

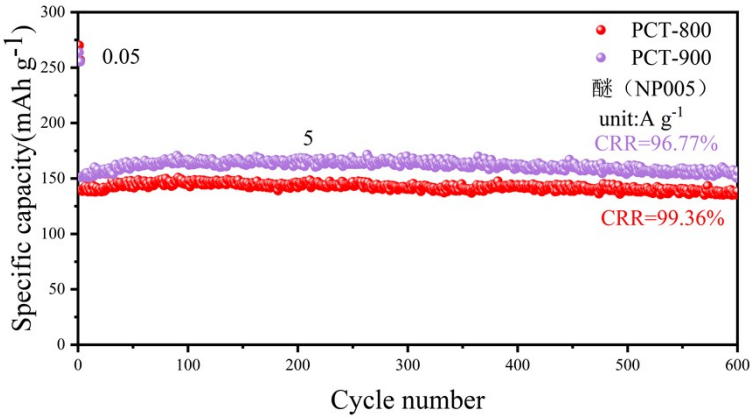

Figure S14. Cycling performance at 5 A g^{-1}.

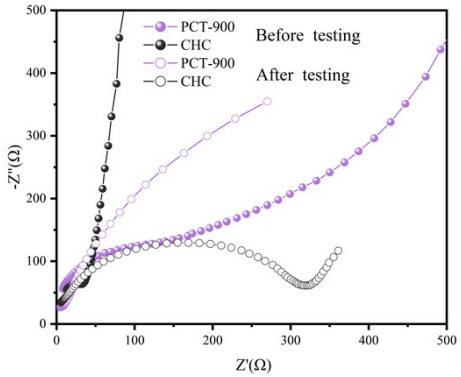

Figure S15. EIS curves of the PCT-900 and CHC before and after cyclic testing.

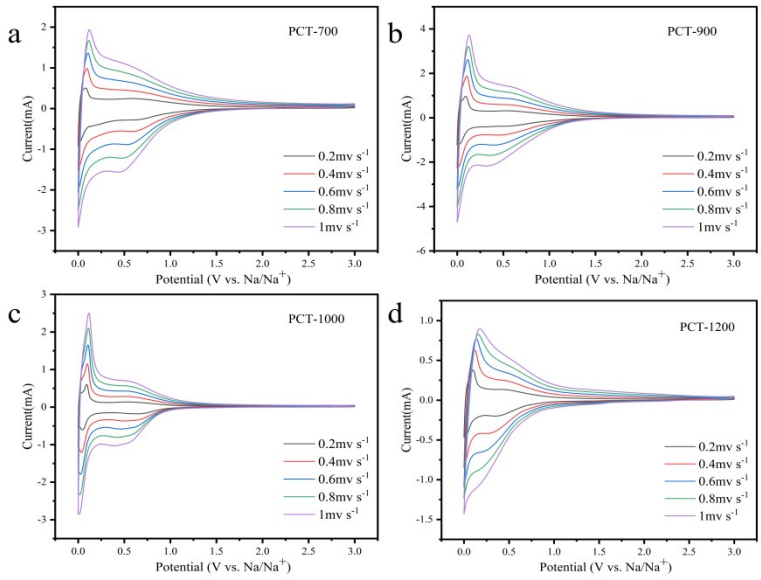

Figure S16. CV curves of (a) PCT-700; (b) CT-900; (c) PCT-1000; (d) PCT-1200.

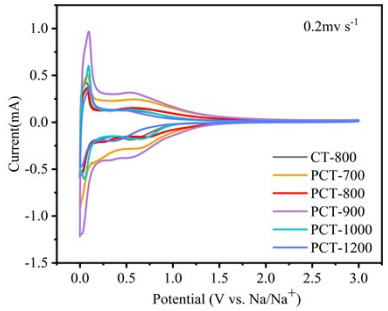

Figure S17. CV curves of PCT-X.

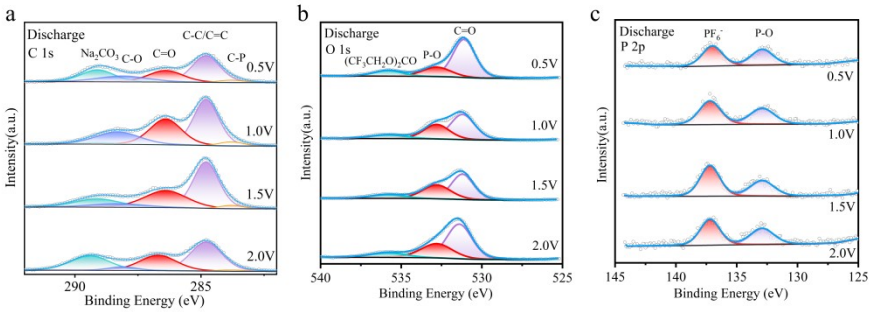

Figure S18. (a-c) PCT-800 anode C 1s, O 1s, and P 2p spectra at different voltages during discharging.

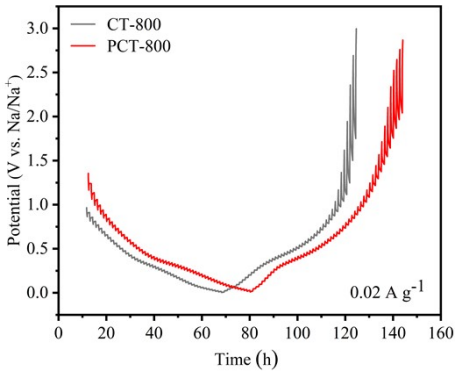

Figure S19. GITT curves of CT-800 and PCT-800.

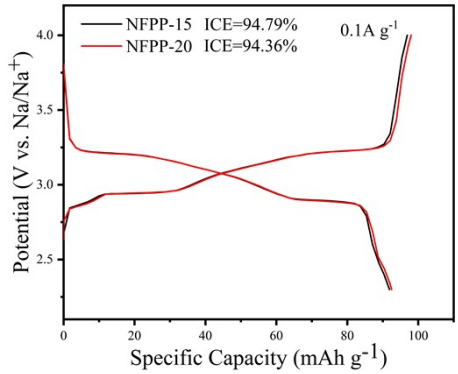

Figure S20. Half-cell performance of NFPP cathode.

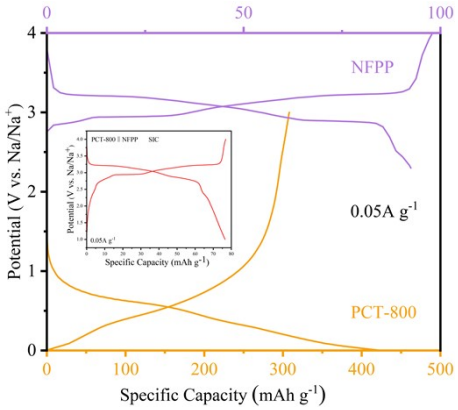

Figure S21. GCD curves of sodium ion capacitor and its cathode and anode.

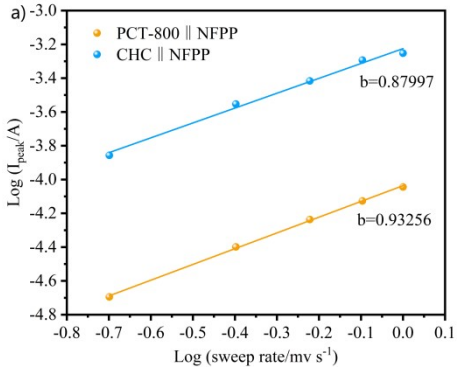

Figure S22. Comparison of the b-value PCT-700.

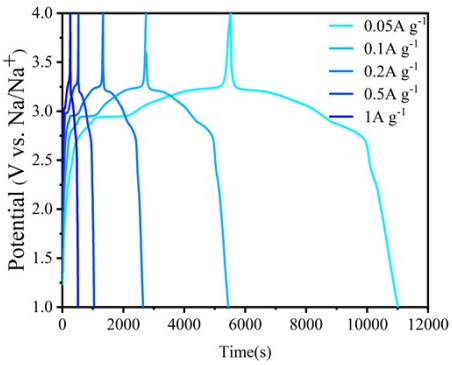

Figure S23. V-t curves of SIC (PCT-800 ‖ NFPP).

Figure S24. Voltage of a single PC (PCT-800 ‖ NFPP) after the formation process.

Figure S25. Voltage of PCs in series connection after 100 cycles of cycling test.

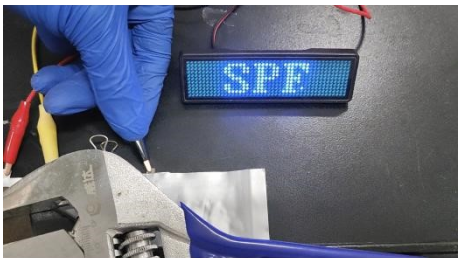

Figure S26. Light up the sign by PCs in series connection.

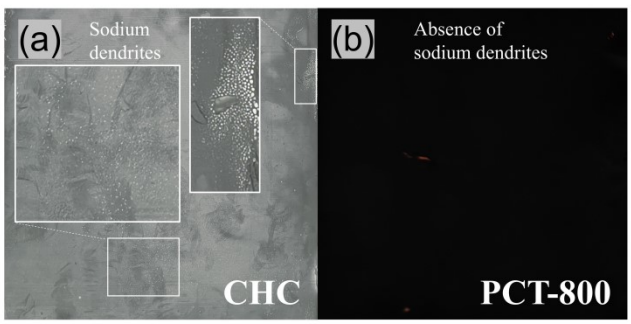

Figure S27. (a-b) The sodium dendrite growth on samples CHC and PCT-800 after fast charging and discharging cycling at a high rate of 30 C.

Table S1. Comparison of the electrochemical performance of coal-based derived carbon anode materials for SIBs.

Precursor	ICE(%)	Reversible capacity (mAh g^{-1}@ mA g^{-1})	Rate capability (mAh g^{-1}@ A g^{-1})	References
Coal tar pitch	67.5	276.8@30	100@0.6	[1]
Raw coal	-	303.1@50	114@10	[2]
Coal pitch	-	313.6@100	131.5@10	[3]
Bitumite	-	306.3@30	100@1	[4]
Anthracite	83.25	220@100	140@1	[5]
Semicoke	81	302.6@30	68.7@1	[6]

Table S2. XRD-related parameters of soft carbon series samples

Sample	$2\theta_{002}$/°	$2\theta_{100}$/°	β_{002}/°	β_{100}/°	L_a/nm	L_c/nm	d_{002}/nm
PCT-700	25.84	43.53	5.30	4.73	7.42	1.58	0.3445
PCT-800	24.82	43.43	6.35	5.01	5.73	1.25	0.3584
PCT-900	25.18	43.80	5.58	5.56	15.52	1.41	0.3534
PCT-1000	25.2	43.89	5.12	5.01	32.92	1.53	0.3531
PCT-1200	25.54	43.89	3.80	4.10	40.51	2.11	0.3485
PCT-1400	25.72	43.65	2.58	3.28	14.64	3.18	0.3461
PCT	25.84	43.19	3.82	3.92	5.20	2.19	0.3445
CT-800	25.3	43.26	6.19	4.59	4.84	1.27	0.3517

Table S3. PCT-800 sample tap density test table

sample	mass/g	tap density/g cm^{-3}	condition
PCT-	0.5311	1.2621	2000 times (250n/min)/amplitude 3mm

800			
CHC	0.5275	0.8095	2000 times (250n/min)/amplitude 3mm

Table S4. Microstructural parameters of PCT-X

Sample	L_a/nm	L_c/nm	d_{002}/nm	I_D/I_G	S_{BET} (m^2/g)	C_{wt}/%	O_{wt}/%	P_{wt}/%
PCT-700	7.42	1.58	0.3445	2.514	3.1013	82.88	14.51	2.61
PCT-800	5.73	1.25	0.3584	2.485	8.7749	85.19	11.56	3.24
PCT-900	15.52	1.41	0.3534	1.931	3.2906	85.68	10.55	3.77
PCT-1000	32.92	1.53	0.3531	1.453	3.7438	88.65	9.19	2.16
CT-800	4.84	1.27	0.3517	2.035	1.5408	93.20	6.80	0
PCT	5.20	2.19	0.3445	2.925	0.1567	46.91	42.9	10.2

Table S5. Comparison of the energy density in SICs

Precursor	Energy density (Wh kg^{-1}@ W kg^{-1})	References
Graphene	60@3000	[7]
N-doped carbon nanofibers	97.8@4118.3	[8]
Semicoke	154@8485	[9]
Fresh juice	52.2@3000	[10]
Pyrrole	168@2432	[11]
Graphene	121.3@8000	[12]
Tetrasodium ethylenediaminetetraacetate tetrahydrate	115@200	[13]
Methyl cellulose	105.6@714	[14]
Phenol-furfural resins	160.2@110.9	[15]
Carbon nanospheres	181.1@5800	[16]

Sodium citrate	179@7200	[17]
Coal tar	197@2892	This Work

References

1 L. Ji, Y. Zhao, L. Cao, Y. Li, C. Ma, X. Qi, Z. Shao, A fundamental understanding of structure evolution in the synthesis of hard carbon from coal tar pitch for high-performance sodium storage, *Journal of Materials Chemistry A*, 2023, **11**, 26727-26741.

2 R. Ma, Y. Chen, Q. Li, B. Zhang, F. Chen, C. Leng, D. Jia, N. Guo, L. Wang, Oxygen-driven closing pore formation in coal-based hard carbon for low-voltage rapid sodium storage, *Chemical Engineering Journal*, 2024, **493**, 152389.

3 S. Wei, X. Deng, W. Li, K. Liu, J. Wang, H. Zhao, X. Wang, Recyclable molten-salt-assisted synthesis of N-doped porous carbon nanosheets from coal tar pitch for high performance sodium batteries, *Chemical Engineering Journal*, 2023, **455**, 140540.

4 R. Li, B. Yang, A. Hu, B. Zhou, M. Liu, L. Yang, Z. Yan, Y. Fan, Y. Pan, J. Chen, T. Li, K. Li, J. Liu, J. Long, Heteroatom screening and microcrystal regulation of coal-derived hard carbon promises high-performance sodium-ion batteries, *Carbon*, 2023, **215**, 118489.

5 H. Ma, Y. Tang, B. Tang, Y. Zhang, L. Deng, L. Liu, S. Dong, Y. Cao, Enhancing the electrochemical performance of semicoke-based hard carbon anode through oxidation-crosslinking strategy for low-cost sodium-ion batteries, *Carbon Energy*, 2024, **6**, e584.

6 J. Liu, Y. You, L. Huang, Q. Zheng, Z. Sun, K. Fang, L. Sha, M. Liu, X. Zhan, J. Zhao, Y. C. Han, Q. Zhang, Y. Chen, S. Wu, L. Zhang, Precisely Tunable Instantaneous Carbon Rearrangement Enables Low-Working-Potential Hard Carbon Toward Sodium-Ion Batteries with Enhanced Energy Density, *Advanced Materials*, 2024, **36**, 2407369.

7 G. Moreno-Fernández, M. Granados-Moreno and D. J. C. Carriazo, High Performance Sodium-Ion Hybrid Capacitor Based on Graphene-Tin Pyrophosphate Nanocomposite Anode, *ChemElectroChem*, 2025, **12**, e202400582.

8 J. Yuan, D. Pan, Z. Bo, Y. Liu, J. Yu, L. Xu, H. Zhan, X. Hu and Z. J. A. A. E. M. Wen, Encapsulation of VC Nanodots within N-Doped Carbon Nanofibers as a Robust and Capacitive Anode for Advanced Sodium-Ion Capacitors, *ACS Applied Energy Materials*, 2025, **8**, 4733-4744.

9 H. Ma, Y. Tang, B. Tang, Y. Zhang, L. Deng, L. Liu, S. Dong and Y. Cao, Enhancing the electrochemical performance of semicoke-based hard carbon anode through oxidation-crosslinking strategy for low-cost sodium-ion batteries, *Carbon Energy*, 2024, **6**, e584.

10 S. Wang, R. Wang, Y. Zhang, D. Jin and L. J. J. o. P. S. Zhang, Scalable and sustainable synthesis of carbon microspheres via a purification-free strategy for sodium-ion capacitors, *Journal of Power Sources*, 2018, **379**, 33-40.

11 F. Wang, X. Wang, Z. Chang, X. Wu, X. Liu, L. Fu, Y. Zhu, Y. Wu and W. J. A. M. Huang, A Quasi-Solid-State Sodium-Ion Capacitor with High Energy Density, *Advanced Materials*, 2015, **27**, 6962-6968.

12 S. Dong, Y. Xu, L. Wu, H. Dou and X. J. E. S. M. Zhang, Surface-functionalized graphene-based quasi-solid-state Na-ion hybrid capacitors with excellent performance, *Energy Storage Materials*, 2018, **11**, 8-15.

13 K. Zou, P. Cai, C. Liu, J. Li, X. Gao, L. Xu, G. Zou, H. Hou, Z. Liu and X. J. J. o. M. C. A. Ji, A kinetically well-matched full-carbon sodium-ion capacitor, *Journal of Materials Chemistry A*, 2019, **7**, 13540-13549.

14 W. Ren, Y. Xiong, L. Yang, Y. Zhang, H. Liang, C. Zhu, X. Wang, J. Chen, W. Tian and M. J. C. Huang, Sulfur modulated oxygen-rich porous carbon exhibiting high-capacity as cathode for sodium ion hybrid

capacitors, *Carbon*, 2025, **238**, 120245.

15 C. Zhang, J. Xu, X. Xiao, Q. Yao, M. Huang, Y. Miao, J. Yao, N. Hu, Z. Guan and D. J. A. F. M. Wang, Rational Precursor Crosslinking Engineering for High-Performance Dual-Carbon Sodium-Ion Capacitors with Optimized Graphitic Microdomains and Pore Structures, *Advanced Functional Materials*, 2025, e14894.

16 G. Su, H. Hou, F. Zeng, B. Liao, K. Zhang, M. Xie, D. Ma, H. Huang and Y. J. C. Pan, Kinetic matching and P-vacancy enrichment of amorphous Ni/Mo–P via central atom modulation in carbon nanospheres for enhanced sodium-ion storage in hybrid capacitors, *Carbon*, 2025, **238**, 120260.

17 H. Chao, H. Liang, X. Luo, Z. Shi, P. Liu, Y. Zhou and J. J. C. E. J. Zhang, Ultrafast laser carbonization endowing high defect density in porous carbon electrode for tunable nitrogen-doping towards high performance sodium storage, *Chemical Engineering Journal*, 2025, **507**, 160456.